One- versus two-degree-of-freedom vortex-induced vibrations of a circular cylinder at Re=3900

Simon Gsell, Rémi Bourguet, Marianna Braza

One- versus two-degree-of-freedom vortex-induced vibrations of a circular cylinder at $Re = 3900$

Simon Gsell [a], Rémi Bourguet [b,*], Marianna Braza [b]

[a] *Aix Marseille Université, CNRS, Centrale Marseille, M2P2, Marseille, France*
[b] *Institut de Mécanique des Fluides de Toulouse, CNRS, Université de Toulouse, Toulouse, France*

The one- versus two-degree-of-freedom vortex-induced vibrations of a circular cylinder are investigated on the basis of direct numerical simulation results. The Reynolds number, based on the oncoming flow velocity and cylinder diameter, is set to 3900. Three cases are examined: the elastically mounted body is free to oscillate either in the direction aligned with the current (in-line direction; *IL* case), in the direction normal to the current (cross-flow direction; *CF* case), or in both directions (*IL+CF* case). In each case, the behavior of the flow–structure system is studied over a range of values of the reduced velocity (inverse of the oscillator natural frequency). The in-line and cross-flow responses observed in the *IL+CF* case substantially differ from their one-degree-of-freedom counterparts, especially in the intermediate reduced velocity region. In this region, no vibrations develop in the *IL* case and in-line oscillations only occur if cross-flow motion is allowed. These in-line oscillations are accompanied by a major increase of the cross-flow responses, compared to the *CF* case. The two-degree-of-freedom vibrations are associated with the emergence of large-amplitude higher harmonics in the fluid force spectra. These aspects and more specifically the impact of the existence of a degree-of-freedom and oscillations in a given direction, on the fluid force and structural response in the perpendicular direction, do not seem to be systematically connected to changes in wake topology. Here, they are discussed in light of the orientation and magnitude of the instantaneous flow velocity seen by the moving body.

1. Introduction

Vortex shedding downstream of a bluff body immersed in a cross-flow is accompanied by unsteady fluid forces exerted on the body. If the body is flexible or flexibly mounted, these forces may lead to structural vibrations, called vortex-induced vibrations (VIV). VIV occur when the body oscillation and the unsteady wake synchronize, a mechanism referred to as lock-in. Many natural and industrial systems are subjected to VIV. Their physical analysis and prediction have motivated a number of research works, as reviewed by Bearman (1984), Sarpkaya (2004), Williamson and Govardhan (2004) and Païdoussis et al. (2010).

Even though most of real systems subjected to VIV involve slender flexible bodies (e.g. chimneys, marine risers), this phenomenon has been extensively studied through the canonical problem of a rigid circular cylinder mounted on an elastic support allowing oscillations in the cross-flow direction (i.e. perpendicular to the oncoming flow), the direction along

* Corresponding author.
E-mail address: remi.bourguet@imft.fr (R. Bourguet).

https://doi.org/10.1016/j.jfluidstructs.2019.01.006
0889-9746/

which large oscillation amplitudes are generally expected (e.g. Huera-Huarte and Bearman, 2009). Through this simplified configuration, VIV can be analyzed with a limited number of structural parameters and a single structural mode (e.g. Feng, 1968; Hover et al., 1998; Khalak and Williamson, 1999; Govardhan and Williamson, 2000; Blackburn et al., 2001; Shiels et al., 2001; Leontini et al., 2006). Significant body oscillations are known to occur over a well-defined range of values of the reduced velocity, defined as the inverse of the oscillator natural frequency non-dimensionalized by the inflow velocity and body diameter. In this range called the lock-in range, the oscillation frequency coincides with wake frequency. The body response amplitude exhibits a bell-shaped evolution as a function of the reduced velocity. Peak amplitudes of the order of one body diameter can be observed, depending on the structural properties (Khalak and Williamson, 1997) and Reynolds number (Re), based on the oncoming flow velocity and body diameter (Govardhan and Williamson, 2000).

The response of an elastically mounted cylinder restricted to move in the in-line direction (i.e. parallel to the oncoming flow) has also been addressed in prior studies (Aguirre, 1977; Naudascher, 1987; Okajima et al., 2004; Cagney and Balabani, 2013). In-line oscillations are known to occur over a range of lower reduced velocities, compared to the typical lock-in range associated with cross-flow VIV. The evolution of the response amplitude as a function of the reduced velocity is characterized by two bell-shaped branches, separated by a region of low-amplitude oscillations. The peak amplitudes are comparable in both branches; they are typically of the order of 0.1 body diameters.

Recently, more attention has been paid to the case where the body is allowed to oscillate in both the in-line and cross-flow directions. Cagney and Balabani (2014) studied the two-degree-of-freedom VIV of a cylinder in the low reduced velocity region, where in-line oscillations occur for a single-degree-of-freedom system. No cross-flow oscillations appear in the first branch of in-line oscillations. In the second branch, cross-flow oscillations develop with amplitudes similar to those noted in the in-line direction. In both branches, the in-line response is almost unaltered compared to that observed for a single-degree-of-freedom system. The effect of adding a degree of freedom in the in-line direction on the system behavior for higher reduced velocities, i.e. where cross-flow oscillations are expected to occur, has been examined by Jauvtis and Williamson (2004). When the structural mass and damping are small, large-amplitude in-line oscillations are superimposed to the cross-flow responses, and the body typically exhibits figure-eight-shaped trajectories, as also confirmed by several studies (Dahl et al., 2010; Navrose and Mittal, 2013; Gsell et al., 2016). The in-line oscillations are accompanied by an increase of the cross-flow oscillation amplitudes, compared to the one-degree-of-freedom case.

The behaviors of the one- and two-degree-of-freedom systems have been widely studied but most of prior works have considered each system separately. The present study aims at a joint analysis of these system responses, over a range of reduced velocities. Among other aspects, the alteration of the in-line vibrations in the intermediate reduced velocity range, and the evolutions of fluid force statistics and frequency content, when adding/removing a degree of freedom to the system, still need to be investigated. More generally, several connections between the in-line and cross-flow responses remain to be clarified.

In the present work, the behaviors of three distinct systems where the cylinder is free to oscillate either in the in-line direction, in the cross-flow direction, or in both directions, are examined over an interval of reduced velocities encompassing the region of cross-flow VIV. The Reynolds number is set to 3900 as a typical case of the early turbulent regime. The comparison between the structural responses, fluid forces and wake patterns observed for the one- and two-degree-of-freedom systems is based on direct numerical simulation results. Particular attention is paid to the relative impact of the in-line and cross-flow oscillations on fluid forces and simple mechanisms are proposed to shed some light on the responses of the two-degree-of-freedom system.

The paper is organized as follows. The methodology employed in this study is presented in Section 2. The behaviors of the three systems are described Section 3. Some elements concerning in-line/cross-flow motion interaction and forcing are discussed in Section 4. The principal findings of this work are summarized in Section 5.

2. Method

The physical systems are described in Section 2.1. The numerical method and data processing approach are presented in Section 2.2. The tools employed to analyze fluid forces are introduced in Section 2.3.

2.1. Physical systems

A sketch of the physical configuration is presented in Fig. 1(a). An elastically mounted, rigid circular cylinder of diameter D and mass per unit length ρ_c is immersed in a cross-flow. The cylinder axis is parallel to the z axis. The flow, parallel to the x axis, is characterized by its velocity U, density ρ_f and dynamic viscosity μ. The Reynolds number based on U and D, $Re = \rho_f UD/\mu$, is set to 3900. The flow dynamics is governed by the three-dimensional incompressible Navier–Stokes equations. The cylinder is elastically mounted and free to oscillate either in the in-line direction (x axis), in the cross-flow direction (y axis), or in both directions, as schematized in Fig. 1(b); the three distinct cases are referred to as IL, CF and $IL{+}CF$, respectively. The structural stiffness and damping ratio in the i (x or y) direction are designated by k_i and γ_i. All the physical quantities are made non-dimensional by D, U and ρ_f. The non-dimensional cylinder displacement, velocity and acceleration in the i direction are denoted by ζ_i, $\dot{\zeta}_i$ and $\ddot{\zeta}_i$. The force coefficient in the i direction is defined as $C_i = 2F_i/\rho_f DU^2$, where F_i

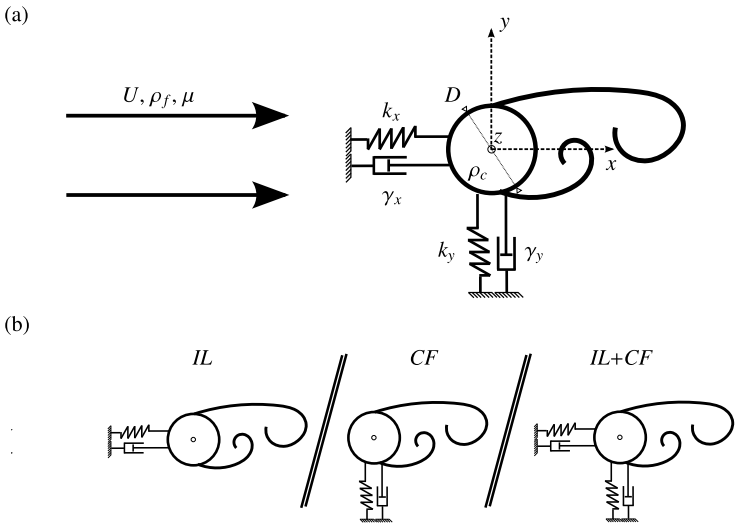

Fig. 1. Sketch of the physical configuration: (a) general two-degree-of-freedom system, and (b) three cases addressed in this paper, where the cylinder is allowed to oscillate in the in-line direction (*IL*), in the cross-flow direction (*CF*), or in both directions (*IL*+*CF*).

denotes the span-averaged force in the i direction. The non-dimensional mass is defined as $m = \rho_c/\rho_f D^2$; it is set to 2. The body dynamics in the i direction is governed by a forced second-order oscillator equation:

$$\ddot{\zeta}_i + \frac{4\pi\gamma_i}{U_i^*}\dot{\zeta}_i + \left(\frac{2\pi}{U_i^*}\right)^2 \zeta_i = \frac{C_i}{2m}. \tag{1}$$

The reduced velocity in the i direction is defined as $U_i^* = 1/f_{nat,i}$, where $f_{nat,i}$ is the natural frequency in vacuum, $f_{nat,i} = D/2\pi U\sqrt{k_i/\rho_c}$. In the one-degree-of-freedom cases (*IL* and *CF*), the reduced velocity U_i^* is denoted by U^*, and the natural frequency $f_{nat,i}$ by f_{nat}. In the two-degree-of-freedom case (*IL*+*CF*), the structural stiffnesses are the same in both directions; the reduced velocity and natural frequency of the oscillator are referred to as $U^* = U_x^* = U_y^*$ and $f_{nat} = f_{nat,x} = f_{nat,y}$. The damping ratio is set equal to zero in both directions to allow maximum amplitude oscillations ($\gamma_i = 0$).

2.2. Numerical method and data processing

The behavior of the coupled flow–structure system is predicted by direct numerical simulation of the three-dimensional Navier–Stokes equations. The numerical procedure is identical to that employed in Gsell et al. (2016). The computations are performed using the finite-volume code Numeca Fine/Open (www.numeca.com), which is based on second-order spatial schemes and a second-order dual-time-stepping time integration. The Navier–Stokes equations are expressed in the cylinder frame which avoids any grid deformation. The frame motion is taken into account by adding inertial terms in the Navier–Stokes equations. At each physical time step, the body motion equations (1) are solved implicitly through a dual-time-stepping scheme. Flow and body solutions are therefore updated simultaneously.

A detailed convergence study has been performed in order to set the numerical parameters, as reported in Gsell et al. (2016). The flow is discretized on a non-structured grid in a rectangular computational domain. The streamwise (x), cross-flow (y) and spanwise (z) lengths of the domain, non-dimensionalized by D, are 120, 60 and 3. Periodic boundary conditions are used in the spanwise and cross-flow directions. The grid size in the wall-normal direction at the cylinder surface is $\Delta n = 1.5 \times 10^{-3}$. In the spanwise direction, 80 cells are considered. The total number of cells is equal to 11.5×10^6.

All the computations are initialized with a static body. The reliability of the simulation approach was assessed in Gsell et al. (2016), where the two-degree-of-freedom system responses and associated fluid forces were found to be close to the experimental results of Jauvtis and Williamson (2004). Additional elements of validation can be found in Section 3.1 for the *CF* case: the present simulation results match the experimental data reported by Hover et al. (1998) for a similar physical system.

The physical quantities are analyzed over time series of more than 20 oscillation cycles, collected after convergence of the structural response. The maximum amplitude of a time-dependent signal s, denoted by s^m, is defined as the average of the highest 10% of its amplitudes. The time-averaged value of s is denoted by $\bar{s}$, and $\tilde{s} = s - \bar{s}$ designates the fluctuating part of s. The root-mean-square (RMS) value of $\tilde{s}$ is denoted by s'. The dominant frequency of the body response in the i direction, based on the Fourier transform of ζ_i time series, is denoted by f_i. The frequency ratio is defined as $f_i^* = f_i/f_{nat}$. As in Gsell et al. (2016), the signals were high-pass filtered in order to avoid low-frequency fluctuations which are not occurring through lock-in. A span and phase averaging procedure of the flow quantities is employed to determine the wake patterns in Section 3.3. The phase averaging is performed over 4 oscillation cycles. For each cycle, a series of 5 snapshots close to the targeted phase are selected. The phase-averaged fields are thus computed with 20 snapshots.

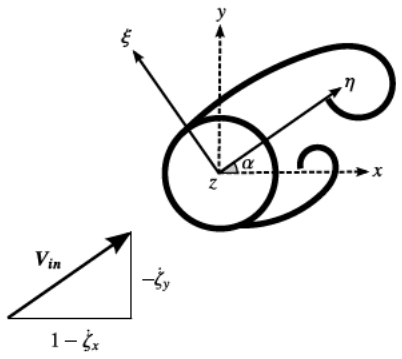

Fig. 2. Sketch of the (η, ξ, z) frame, aligned with the instantaneous flow seen by the moving body.

2.3. Fluid force analysis and modeling

Two tools are introduced to analyze the fluid forces exerted on the moving body (Section 4): a projection of the forces in a frame aligned with the instantaneous flow seen by the cylinder, and a simple, phenomenological modeling of the forces expressed in this new frame.

The new frame (η, ξ, z) is schematized in Fig. 2. The η axis (ξ axis, respectively) is parallel (normal, respectively) to the instantaneous oncoming flow velocity $\boldsymbol{V_{in}}$, defined as $\boldsymbol{V_{in}} = [V_{in,x}, V_{in,y}, 0] = [1 - \dot{\zeta}_x, -\dot{\zeta}_y, 0]$. The angle between the x axis and the η axis, denoted by α, is determined by the body velocity:

$$\alpha = \arctan2\left(-\dot{\zeta}_y, 1 - \dot{\zeta}_x\right). \tag{2}$$

The fluid force coefficients in the η and ξ directions, C_η and C_ξ, are connected to the fluid forces along the x and y axes as follows:

$$C_x = C_\eta \cos(\alpha) - C_\xi \sin(\alpha), \tag{3a}$$

$$C_y = C_\eta \sin(\alpha) + C_\xi \cos(\alpha). \tag{3b}$$

In order to suggest some possible connections between the physical quantities, a simple model of C_η and C_ξ is proposed in the following. It should be mentioned that the object of this phenomenological model is not to provide an accurate prediction of the forces but to shed some light on the possible modulations induced by the variations of the flow velocity seen by the body. The model assumes that C_η and C_ξ can be expressed as force coefficients, denoted by C_x^f and C_y^f, whose global forms are comparable to those observed in the fixed body case (i.e. mean in-line component, frequency ratio of 2 between in-line and cross-flow components), altered by the instantaneous flow velocity:

$$C_\eta \approx \left[1 + \kappa_\eta(\Psi - 1)\right] C_x^f, \tag{4a}$$

$$C_\xi \approx \left[1 + \kappa_\xi(\Psi - 1)\right] C_y^f, \tag{4b}$$

where Ψ is the square of the instantaneous flow velocity magnitude, $\Psi = |\boldsymbol{V_{in}}|^2$, which can be expressed as a function of the body velocity,

$$\Psi = (1 - \dot{\zeta}_x)^2 + \dot{\zeta}_y{}^2, \tag{5}$$

and C_x^f and C_y^f are defined as follows,

$$C_x^f = \overline{C_x^f} + C_{x,2}^f \sin(4\pi f_1 t + \phi_{C_{x,2}^f}), \tag{6a}$$

$$C_y^f = C_{y,1}^f \sin(2\pi f_1 t + \phi_{C_{y,1}^f}). \tag{6b}$$

In the above expressions, t denotes the time variable and f_1 the dominant frequency of the wake unsteadiness and body oscillations, which are synchronized under the lock-in condition; $C_{i,n}^f$ and $\phi_{C_{i,n}^f}$ are the amplitude and phase of the nth harmonic of the force coefficient in the i direction. The model (4) is inspired by the quasi-steady approach (i.e. modulation by the square of the instantaneous velocity magnitude) but it does not assume a quasi-steady evolution of the forces with respect to body motion; in particular, the forces do not necessarily vanish when the instantaneous oncoming flow velocity vanishes (i.e. when $\Psi = 0$). That is why the values of the coefficients κ_η and κ_ξ are a priori unknown and may differ from 1. It is however expected that κ_η and κ_ξ remain positive since fluid forces are generally amplified when the oncoming flow velocity increases. This observation is supported by the results presented in Section 4.

Neglecting higher harmonic terms, the square of the instantaneous flow velocity magnitude can be expressed as follows:

$$\Psi \approx \overline{\Psi} + \Psi_2 \sin(4\pi f_1 t + \phi_{\Psi_2}), \tag{7}$$

where Ψ_2 and ϕ_{Ψ_2} denote the amplitude and phase of the second harmonic of Ψ. Combining expressions (4), (6) and (7), the fluid force coefficients in the η and ξ directions can be modeled as follows:

$$\begin{aligned} C_\eta \approx & \left[1 + \kappa_\eta(\overline{\Psi} - 1)\right]\overline{C_x^f} + \frac{1}{2}\kappa_\eta \Psi_2 C_{x,2}^f \cos(\phi_{\Psi_2} - \phi_{C_{x,2}^f}) \\ & + \kappa_\eta \overline{C_x^f} \Psi_2 \sin(4\pi f_1 t + \phi_{\Psi_2}) + \left[1 + \kappa_\eta(\overline{\Psi} - 1)\right] C_{x,2}^f \sin(4\pi f_1 t + \phi_{C_{x,2}^f}) \\ & - \frac{1}{2}\kappa_\eta \Psi_2 C_{x,2}^f \cos(8\pi f_1 t + \phi_{\Psi_2} + \phi_{C_{x,2}^f}), \end{aligned} \tag{8}$$

and

$$\begin{aligned} C_\xi \approx & \left[1 + \kappa_\xi(\overline{\Psi} - 1)\right] C_{y,1}^f \sin(2\pi f_1 t + \phi_{C_{y,1}^f}) + \frac{1}{2}\kappa_\xi \Psi_2 C_{y,1}^f \cos(2\pi f_1 t + \phi_{\Psi_2} - \phi_{C_{y,1}^f}) \\ & - \frac{1}{2}\kappa_\xi \Psi_2 C_{y,1}^f \cos(6\pi f_1 t + \phi_{\Psi_2} + \phi_{C_{y,1}^f}). \end{aligned} \tag{9}$$

The connections between fluid forces and the two kinematic quantities α and Ψ will be explored in Section 4.

3. Results

The results issued from the numerical simulations for the one- and two-degree-of-freedom systems are reported in this section. The body responses are quantified in Section 3.1, the fluid forces are examined in Section 3.2 and some elements regarding wake topology are presented in Section 3.3.

3.1. Structural responses

The structural responses obtained in the three studied cases (*IL*, *CF* and *IL+CF*) are depicted in Fig. 3. In the *CF* case, the oscillation amplitudes match the experimental data of Hover et al. (1998) for $U^* < 9$ (Fig. 3(a)). The peak amplitude, observed for $U^* = 5$, is approximately equal to 0.8 diameters. For $U^* > 9$, the oscillation amplitudes reported by Hover et al. (1998) decrease down to 0.2 diameters, while relatively large vibrations are still observed in the present numerical results. As shown in Gsell et al. (2016), the body response is particularly sensitive to structural damping in the high reduced velocity region: a small structural damping can substantially decrease the response amplitude in this region. In the experiments of Hover et al. (1998), the structural damping is small but still not negligible; this may explain the differences observed with the present results. The cross-flow oscillation amplitudes obtained in the *IL+CF* case are also reported in Fig. 3(a). The cross-flow response is globally amplified when the in-line degree of freedom is added to the system, as previously noted by Jauvtis and Williamson (2004). The peak oscillation amplitude is lower than the maximum amplitude reported by Jauvtis and Williamson (2004). This may relate to the value of the Reynolds number, which is higher in the experiments as discussed in Gsell et al. (2016). Otherwise, the cross-flow amplitudes remain globally close to the experimental data. The differences noted in the high reduced velocity region can be explained by the above mentioned effect of the structural damping.

The in-line oscillation amplitudes obtained in the *IL* and *IL+CF* cases are plotted in Fig. 3(b). In the *IL+CF* case, the amplitudes match those reported by Jauvtis and Williamson (2004). Small oscillations occur in the low reduced velocity region ($U^* = 3$). This region has been thoroughly analyzed by Cagney and Balabani (2014) for a slightly different system (pivoted cylinder). They found that the in-line vibrations are not impacted by the addition of the cross-flow degree of freedom. This observation is confirmed by the present results. In contrast, at higher reduced velocities, the *IL* and *IL+CF* cases exhibit distinct behaviors: negligible vibrations are noted in the *IL* case, while significant oscillations appear in the *IL+CF* case, especially around $U^* = 6$. In this region, which coincides with the region of peak cross-flow oscillation amplitudes, in-line response amplitudes up to 0.3 diameters are encountered. The in-line vibration amplitude rapidly decreases beyond this region where only residual oscillations persist. The present results suggest that in the *IL+CF* case, the in-line oscillations occurring in the intermediate reduced velocity range are closely connected to the presence of cross-flow motion. This aspect is discussed in Section 4.

Body responses are generally close to harmonic. Their frequencies are quantified in Fig. 3(c) which represents the evolutions of the frequency ratios in both directions, as functions of the reduced velocity. In the *IL* case, the oscillations appearing for $U^* = 3$ occur close to the oscillator natural frequency. The frequency of the oscillations of negligible amplitude noted at higher U^* matches the frequency of the in-line fluid force in the fixed body case, equal to twice the Strouhal frequency (i.e. vortex shedding frequency in the fixed body case, denoted by f_{st} in the plot). In the *CF* case, the oscillation frequency remains close to the Strouhal frequency for $U^* \in [3, 6]$. At higher reduced velocities, f_y^* reaches a plateau, and the oscillation frequency significantly departs from the Strouhal frequency. In the *IL+CF* case, the in-line response frequency is equal to twice the cross-flow response frequency over the range of U^* under study. For $U^* = 3$, the in-line

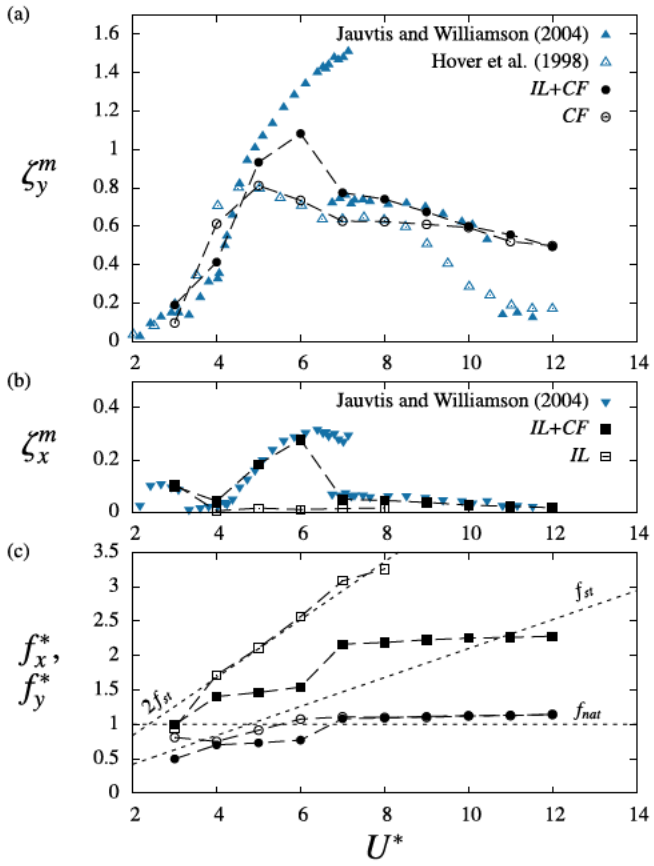

Fig. 3. Structural responses as functions of the reduced velocity, in the three studied cases (*IL*, *CF* and *IL+CF*): (a) cross-flow oscillation amplitude, (b) in-line oscillation amplitude and (c) in-line and cross-flow frequency ratios. In (a) and (b), the present numerical results are compared to the experimental data of Hover et al. (1998) and Jauvtis and Williamson (2004).

response frequency matches that observed in the *IL* case. At higher reduced velocities, the in-line and cross-flow oscillation frequencies follow two clearly-defined branches, each one characterized by a close to constant frequency ratio. In the first branch ($U^* \in [4, 6]$) $f_y^* < 1$, while in the second branch ($U^* > 7$), $f_y^* > 1$ and the cross-flow response frequency ratio coincides to that noted in the *CF* case.

3.2. Fluid forces

Some statistics of the fluid force coefficients obtained in the three studied cases are represented in Fig. 4. When the body is fixed, the time-averaged in-line force coefficient is close to 0.9 (Wieselsberger, 1922), and the RMS values of the fluctuating forces in the in-line and cross-flow directions remain small, i.e. close to 0.03 (Ouvrard et al., 2010; Afgan et al., 2011) and 0.08 (Norberg, 2003), respectively. In the *IL* case, no significant structural oscillations occur for $U^* \geq 4$ (Fig. 3(b)) and the force statistics are close to those observed in the fixed body case. An overview of Fig. 4 shows that the fluid forces are generally amplified when the body oscillates. The differences between the one- and two-degree-of-freedom cases are principally concentrated in the intermediate reduced velocity region ($U^* \in [4, 6]$): for $U^* = 3$, the fluid force statistics in the *IL+CF* case are close to those noted in the *IL* case while for $U^* > 6$, they tend to match those noted in the *CF* case.

In Fig. 4(a), the time-averaged in-line force coefficient is plotted as a function of the reduced velocity. An increase of $\overline{C_x}$ is observed when the body oscillates in the cross-flow direction (*CF* case), as often reported in previous works (e.g. Bishop and Hassan, 1964; Sarpkaya, 1978). This amplification may be connected to an increase of the apparent size of the obstacle as the body oscillates (Khalak and Williamson, 1999). However, the results obtained in the *IL* case for $U^* = 3$ show that small in-line oscillations ($\zeta_x^m \approx 0.1$) are associated with an amplification of $\overline{C_x}$ by a factor of 2, compared to the fixed body case. This suggests a possible influence of the instantaneous flow velocity seen by the moving cylinder. The largest amplification of the time-averaged in-line force is encountered in the *IL+CF* case; for $U^* = 6$, $\overline{C_x}$ is close to 3, i.e. approximately three times the fixed body case value. The connection between body motion, in the in-line and/or cross-flow directions, and $\overline{C_x}$, is further analyzed in Section 4.

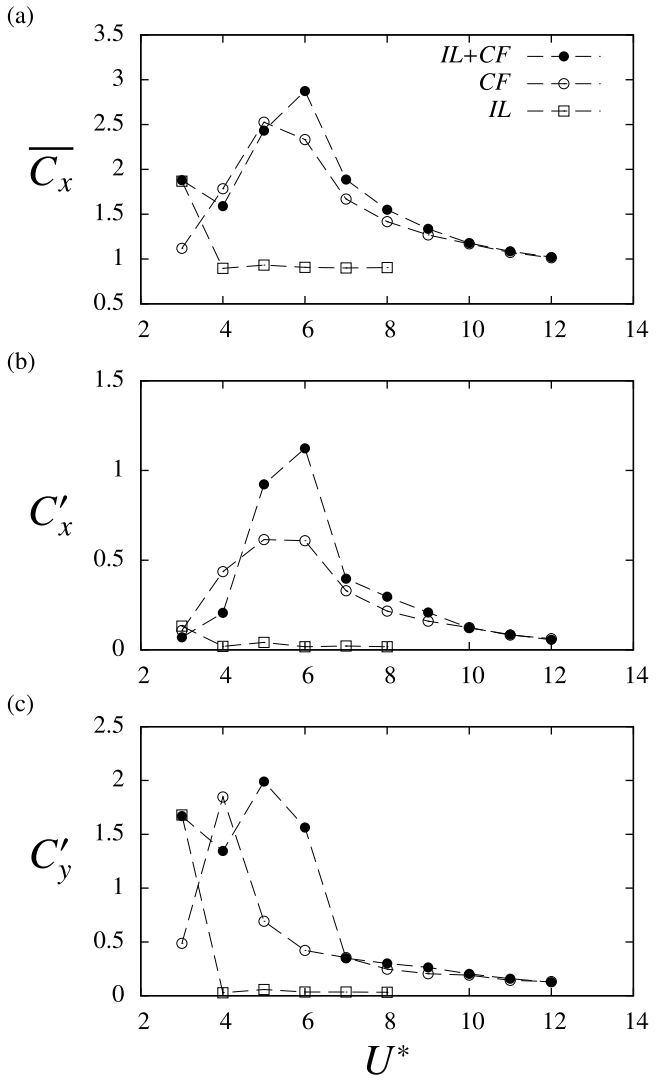

Fig. 4. Fluid force statistics as functions of the reduced velocity, in the three studied cases: (a) time-averaged in-line force coefficient and RMS values of the fluctuating (b) in-line and (c) cross-flow force coefficients.

The RMS value of the fluctuating in-line force coefficient is plotted in Fig. 4(b). The *CF* case results indicate a major amplification of $\widetilde{C_x}$ when the body oscillates in the cross-flow direction, compared to the fixed body case. Such amplification of the in-line force fluctuation is expected to impact the in-line responses when the body is allowed to oscillate in both directions. An increase of C'_x, even though less pronounced than in the *CF* case, is also noted in the *IL* case (for $U^* = 3$). C'_x is generally larger in the two-degree-of-freedom case in the intermediate reduced velocity region. In particular, the peak of C'_x in this region is approximately twice larger in the *IL*+*CF* case than in the *CF* case.

The evolution of C'_y versus U^* is depicted in Fig. 4(c). As shown by the results obtained in the one-degree-of-freedom cases, both in-line and cross-flow oscillations are accompanied by an amplification of $\widetilde{C_y}$. It appears that small-amplitude in-line oscillations can induce a substantial increase of C'_y ($U^* = 3$ in the *IL* case). The cross-flow force fluctuation is often amplified in the *IL*+*CF* case compared to one-degree-of-freedom cases.

Typical time evolutions of the fluid force coefficients are presented in Fig. 5. Selected time series of the force coefficients and their spectral amplitudes based on Fourier transform are plotted for $U^* = 3$ in the *IL* case and $U^* = 6$ in the *CF* and *IL*+*CF* cases, i.e. in the regions of peak oscillation amplitudes. The spectra show that the fluctuating in-line and cross-flow forces are dominated by frequencies equal to $2f_1$ and f_1, respectively; this is generally the case over the parameter space investigated. It is recalled that f_1 denotes the dominant frequency of the wake unsteadiness, synchronized with body oscillations under the lock-in condition. The frequency ratio between the in-line and cross-flow forces is expected due to the symmetry of the system. Higher harmonic components may also emerge. In particular, a third harmonic ($3f_1$) appears in C_y spectrum and a fourth harmonic ($4f_1$) is sometimes noted in C_x spectrum. The contributions of the force higher harmonic components

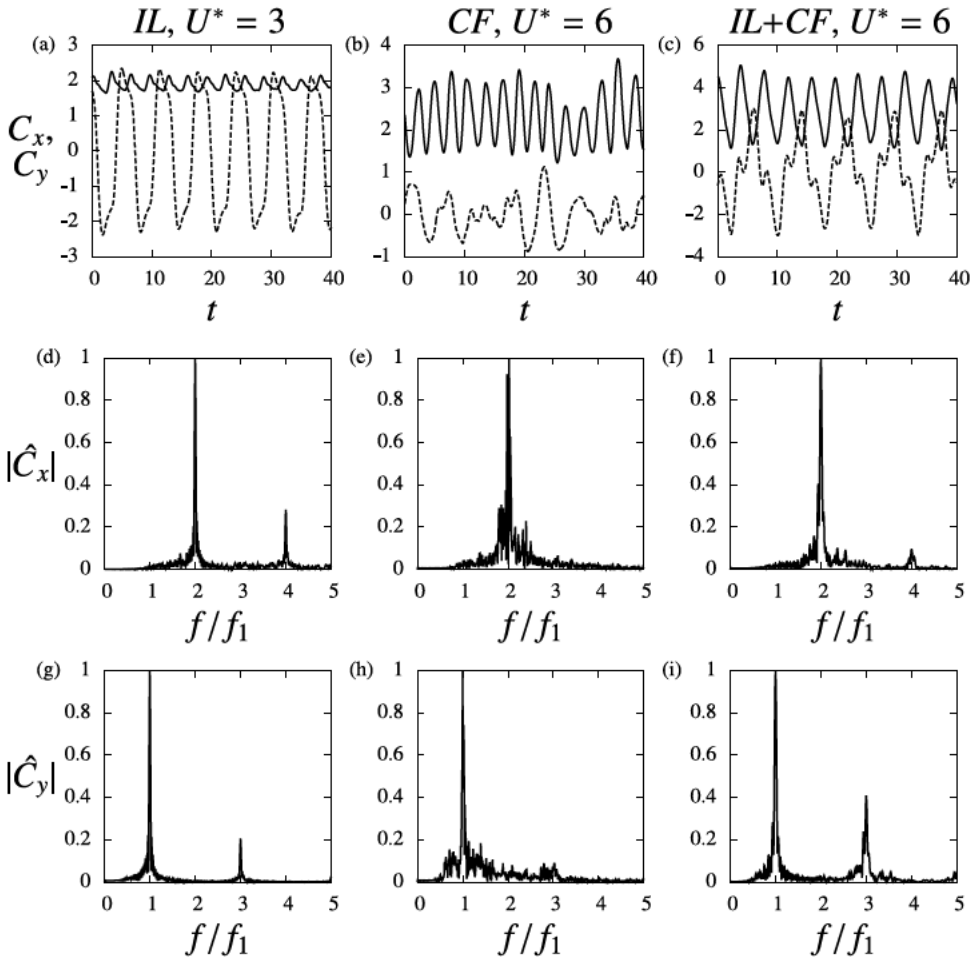

Fig. 5. Typical time evolutions of the fluid force coefficients in the regions of peak oscillation amplitudes: (a–c) selected time series and (d–i) spectral amplitudes of $\widetilde{C_x}$ and $\widetilde{C_y}$, in the (a, d, g) *IL* case ($U^* = 3$), (b, e, h) *CF* case ($U^* = 6$) and (c, f, i) *IL+CF* case ($U^* = 6$). In (d–i), the spectral amplitudes are normalized by the peak amplitude of the spectrum.

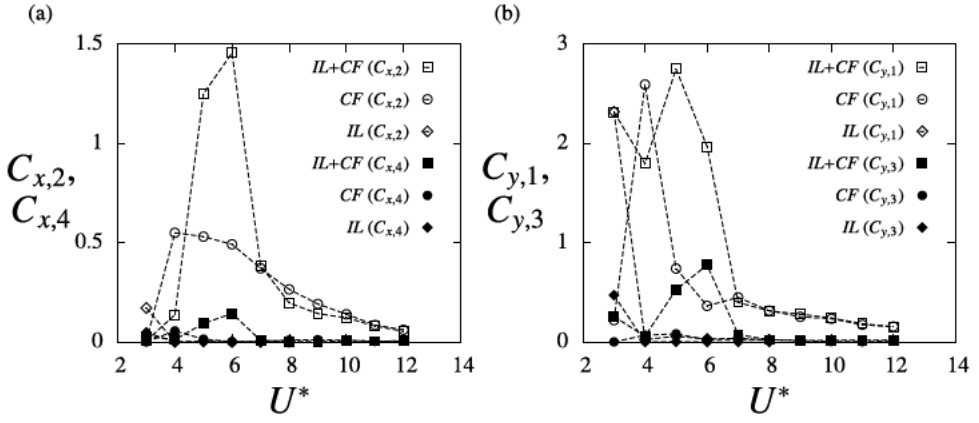

Fig. 6. Amplitudes of the principal spectral components of the fluid forces as functions of the reduced velocity, in the three studied cases: (a) $C_{x,2}$ and $C_{x,4}$, and (b) $C_{y,1}$ and $C_{y,3}$.

significantly vary from one case to the other. In the following, the amplitude of the nth harmonic of the force coefficient in the i direction is denoted by $C_{i,n}$.

The amplitudes of the principal spectral components of the in-line ($C_{x,2}$ and $C_{x,4}$) and cross-flow ($C_{y,1}$ and $C_{y,3}$) forces are plotted in Fig. 6, as functions of the reduced velocity, in the three studied cases. In each direction, the evolution of the dominant spectral component amplitude ($C_{x,2}$ and $C_{y,1}$) is comparable to the evolution of the RMS value of the entire signal (C'_x and C'_y, Fig. 4(b,c)). In the in-line direction (Fig. 6(a)), the magnitude of the fourth harmonic component remains small compared to $C_{x,2}$. An increase of $C_{x,4}$ can however be noted for $U^* = 5$ and $U^* = 6$ in the *IL+CF* case. In the cross-flow direction (Fig. 6(b)), a large-amplitude third harmonic component occurs in the *IL+CF* case, in the intermediate reduced velocity region: for $U^* = 6$, the third harmonic amplitude reaches 40% of the first harmonic amplitude. The *IL* case results for $U^* = 3$ also indicate a significant amplification of the third harmonic when the body oscillates in the in-line direction. On the other hand, $C_{y,3}$ remains negligible in the *CF* case. These observations suggest that the large-amplitude third harmonic noted in the *IL+CF* case may be essentially related to the in-line oscillations of the cylinder; this phenomenon is examined in Section 4.

3.3. Wake patterns

Visualizations of wake patterns encountered in the three studied cases are presented in Fig. 7. They consist of iso-contours of the span- and phase-averaged, spanwise vorticity, for $U^* = 6$, i.e. in the region where body responses and fluid forces significantly differ from one case to the other (Figs. 3, 4 and 6). Two phases are considered for each case. In each plot, the phase-averaged trajectory of the body is indicated as well as its actual position. In the *IL* case (Fig. 7(a, b)), the body is almost stationary and the flow exhibits a typical vortex street pattern, similar to that observed when the body is fixed, where single counter-rotating vortices are alternatively shed. Following the nomenclature introduced by Williamson and Roshko (1988), this flow topology can be referred to as a *2S* pattern. Wake structure is altered when the body oscillates in the cross-flow direction (Fig. 7(c, d)). A *2P* pattern can be identified in this case: two pairs of counter-rotating vortices form per oscillation cycle. This is consistent with prior experimental results reported by Brika and Laneville (1993) and Govardhan and Williamson (2000), in the region of peak oscillation amplitudes. In contrast, a *2S* pattern, globally comparable to that noted in the *IL* case, develops in the *IL+CF* case, which corroborates the observations of Navrose and Mittal (2013), but departs from the visualizations of Jauvtis and Williamson (2004), due to the different Reynolds numbers, as discussed in Gsell et al. (2016).

The topology of the flow may thus vary from one case to the other. However, cases with distinct behaviors, as those observed in the intermediate reduced velocity region, may also exhibit comparable wake patterns: for example large higher harmonic components appear for $U^* = 6$ in the *IL+CF* case but not in the *IL* case, while both cases exhibit a *2S* wake pattern. The differences noted between the *IL+CF* case and its one-degree-of-freedom counterparts, and more generally the interactions between in-line and cross-flow forces/responses, do not seem to be systematically connected to wake topology. Some possible mechanisms driving the contrasted behaviors of the one- and two-degree-of-freedom systems are investigated in the next section.

4. Discussion

The results reported in Section 3 show that the fluid force and body response in a given direction (x or y) may be substantially impacted by the existence of a degree-of-freedom and oscillations in the perpendicular direction (y or x). Three striking features observed in the intermediate reduced velocity region are particularly addressed in this section: (i) in this range of U^*, in-line oscillations only occur if cross-flow motion is allowed (Fig. 3(b)); (ii) cross-flow oscillations are also influenced by the in-line degree of freedom in this region, since an increase of the oscillation peak amplitude is noted between cases *CF* and *IL+CF* (Fig. 3(a)); (iii) concerning fluid forces, large higher harmonic contributions are observed in the cross-flow direction when the body is subjected to both in-line and cross-flow oscillations, while in the *CF* case they remain negligible (Fig. 6(b)).

In the following, these features are discussed in light of the evolutions of the two kinematic quantities introduced in Section 2.3, α and Ψ, which relate to body motion. The angle α is the angle between the x axis and the instantaneous oncoming flow velocity (expression (2)). The evolution of the maximum angle α (α^m) as a function of the reduced velocity is plotted in Fig. 8(a), in the three studied cases. As expected, α vanishes in the *IL* case. Large values of α^m are encountered when cross-flow oscillations occur. In both the *CF* and *IL+CF* cases, the region of peak α^m matches the region of peak oscillation amplitudes (Fig. 3). The values of α^m are generally larger in the *IL+CF* case, where angles up to 0.9 radians ($\approx 50°$) can be noted.

The second kinematic quantity, Ψ, relates to the magnitude of the instantaneous oncoming flow velocity ($\Psi = |\boldsymbol{V_{in}}|^2$). When the cylinder is fixed then Ψ is equal to 1 and it may substantially depart from this value when the body oscillates. A spectral analysis shows that the fluctuating part of Ψ is dominated by its second harmonic component ($2f_1$) so that expression (7) provides a reasonable approximation. The values of $\overline{\Psi}$ and Ψ_2 are plotted in Fig. 8(b) as functions of U^*. In the *IL* case, $\overline{\Psi}$ is almost unaltered when the body oscillates ($U^* = 3$). In contrast, it significantly increases in the *CF* and *IL+CF* cases, especially in the intermediate reduced velocity region. In the *IL+CF* case, a maximum increase of 50% is noted compared the fixed cylinder case. Ψ_2 is also altered when the body oscillates. Both in-line and cross-flow oscillations are associated with an increase of Ψ_2, as shown by the results obtained in the *IL* and *CF* cases. The largest values of Ψ_2 are observed in the two-degree-of-freedom case; in the region of peak oscillation amplitudes ($U^* \approx 6$), Ψ_2 is close to the value of $\overline{\Psi}$ in the fixed body case ($\Psi_2 \approx 1$).

The role of α and Ψ in the alteration of fluid forcing is examined hereafter.

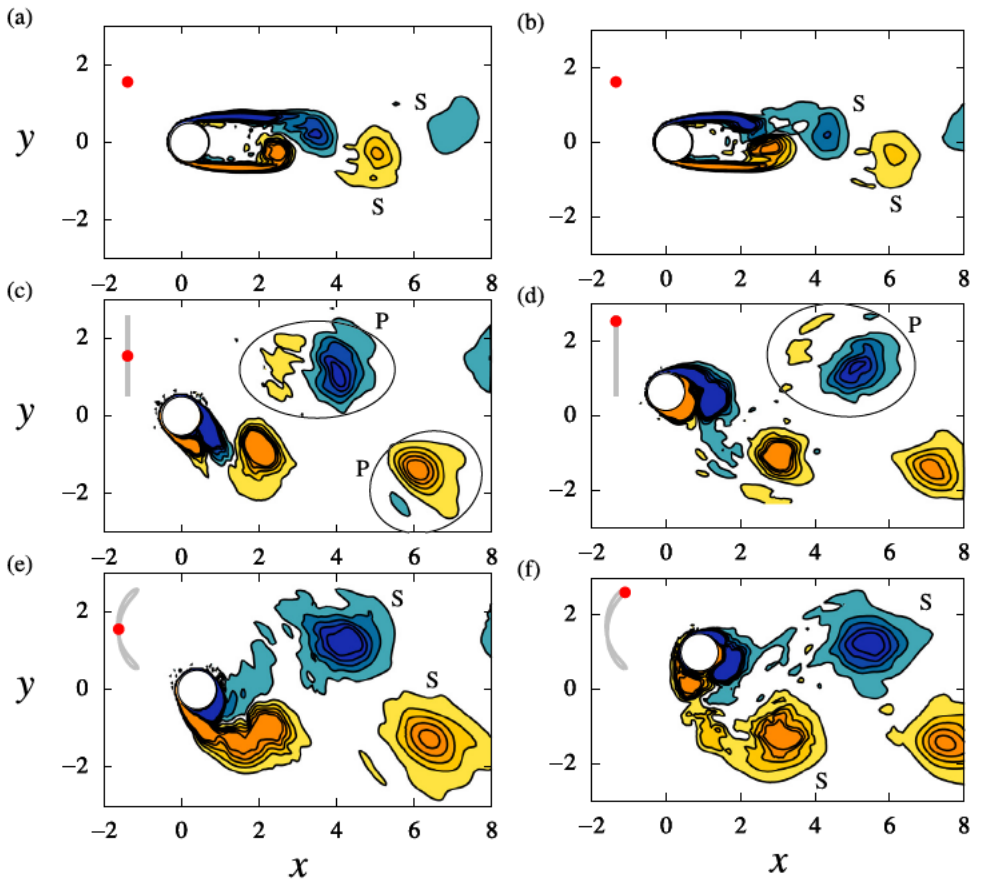

Fig. 7. Wake patterns in the intermediate reduced velocity region ($U^* = 6$), for the three studied cases: iso-contours of span- and phase-averaged spanwise vorticity in the (a, b) *IL*, (c, d) *CF* and (e, f) *IL*+*CF* cases. Two phases are considered for each case. Vorticity contours are linearly distributed in the range $\omega_z \in [-2, 2]$. In each plot, the phase-averaged trajectory of the body is indicated by a gray line and its position is denoted by a red dot. Part of the computational domain is shown.

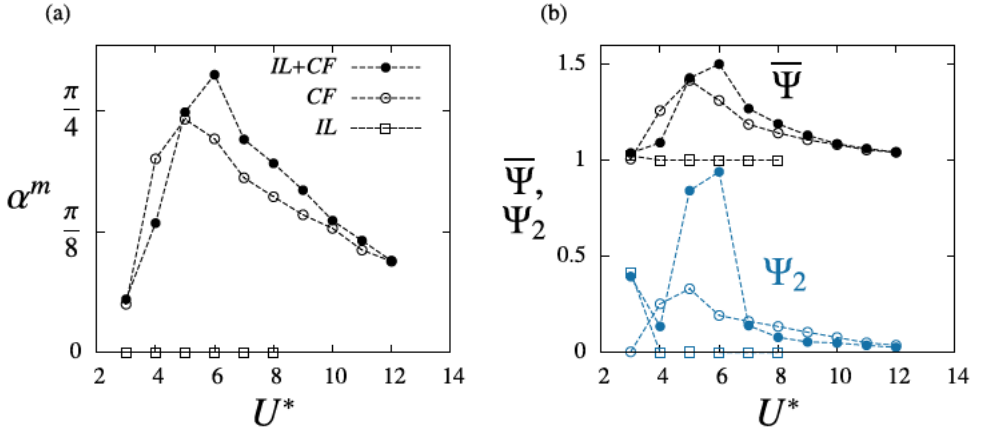

Fig. 8. Kinematic quantities related to body motion as functions of the reduced velocity, in the three studied cases: (a) α^m and (b) $\overline{\Psi}$ and Ψ_2.

4.1. Influence of α

As shown in Section 2.3 (expression (3)), C_x and C_y can be expressed as combined contributions of C_η and C_ξ, which relate to the forces parallel and normal to the instantaneous oncoming flow velocity. The fluid force coefficient in the *i* direction (*x*

or y) can be written as follows:

$$C_i = D_i + L_i, \tag{10}$$

where D_i denotes the drag-like contribution to C_i ($D_x = C_\eta \cos(\alpha)$ and $D_y = C_\eta \sin(\alpha)$), in reference to its alignment with the instantaneous flow velocity, and L_i denotes the lift-like contribution ($L_x = -C_\xi \sin(\alpha)$ and $L_y = C_\xi \cos(\alpha)$), i.e. perpendicular to the instantaneous flow velocity. In the fixed body case and *IL* case, α vanishes, therefore $C_x = D_x$ and $C_y = L_y$. Assuming that C_i, D_i and L_i are periodic functions of time, they can be expressed as Fourier series,

$$C_i = \sum_{n=0}^{\infty} C_{i,n} \sin(2\pi n f_1 t + \phi_{C_{i,n}}), \tag{11a}$$

$$D_i = \sum_{n=0}^{\infty} D_{i,n} \sin(2\pi n f_1 t + \phi_{D_{i,n}}), \tag{11b}$$

$$L_i = \sum_{n=0}^{\infty} L_{i,n} \sin(2\pi n f_1 t + \phi_{L_{i,n}}), \tag{11c}$$

where $C_{i,n}$, $D_{i,n}$ and $L_{i,n}$ are the spectral amplitudes of the nth harmonics, and $\phi_{C_{i,n}}$, $\phi_{D_{i,n}}$ and $\phi_{L_{i,n}}$ the corresponding phases. The amplitude of the nth harmonic of C_i relates to the nth harmonics of D_i and L_i as follows:

$$C_{i,n} = D_{i,n} \cos(\phi_{D_{i,n}} - \phi_{C_{i,n}}) + L_{i,n} \cos(\phi_{L_{i,n}} - \phi_{C_{i,n}}). \tag{12}$$

The results reported in Fig. 4(b) reveal a major amplification of the fluctuating in-line force when the body oscillates in the cross-flow direction. According to (10), this amplification may relate to two effects: an amplification of D_x related to body motion, and the appearance of a lift-like contribution (L_x) induced by the angle α. A spectral analysis of C_x shows that its fluctuating part is dominated by the second harmonic component. According to (12), the magnitude of this harmonic can be expressed as follows:

$$C_{x,2} = D_{x,2} \cos(\phi_{D_{x,2}} - \phi_{C_{x,2}}) + L_{x,2} \cos(\phi_{L_{x,2}} - \phi_{C_{x,2}}). \tag{13}$$

The relative weights of the different terms in (13), issued from the present simulation results, are plotted in Fig. 9, in the *CF* and *IL+CF* cases. In the *CF* case (Fig. 9(a)), the lift-like contribution is clearly dominant, especially in the region of peak amplitudes of $C_{x,2}$. For $U^* = 4$ and $U^* = 5$, the drag-like contribution is even negative: it tends to decrease the amplitude of the in-line force fluctuation. At higher reduced velocities, both contributions are positive but the relative contribution of L_x to $C_{x,2}$ remains larger than 70%. This result suggests that the large amplitude of the fluctuating in-line force noted in Fig. 4(b) in the *CF* case, is mainly related to the emergence of a lift-like contribution associated with the angle α. A comparable behavior is observed in the *IL+CF* case (Fig. 9(b)). A simple mechanism of interaction between the in-line and cross-flow motions can be proposed: as the body moves in the cross-flow direction, a fluctuating lift-like component emerges and considerably alters the amplitude of $\widetilde{C_x}$, and the resulting in-line vibration, if the body is allowed to move in this direction. This may explain why, in the intermediate range of U^*, in-line oscillations appear when cross-flow oscillations occur.

Similarly, the cross-flow force coefficient C_y can be altered by the emergence of a drag-like contribution related to the angle α. According to expression (12), the amplitude of the first harmonic of C_y (which dominates its spectrum) writes

$$C_{y,1} = D_{y,1} \cos(\phi_{D_{y,1}} - \phi_{C_{y,1}}) + L_{y,1} \cos(\phi_{L_{y,1}} - \phi_{C_{y,1}}). \tag{14}$$

An analysis of the relative weights of each term in (14) shows that the drag-like contribution to $C_{y,1}$ is negligible.

4.2. Influence of Ψ

A simple model has been introduced in Section 2.3 to shed some light on the modulations of the fluid forces expressed in the moving frame, due to the variation of the instantaneous flow velocity magnitude. Following this model, the time-averaged value of the force coefficient aligned with the instantaneous flow velocity can be expressed as

$$\overline{C_\eta} \approx (1 - \kappa_\eta)\overline{C_x^f} + \kappa_\eta \overline{C_x^f}\,\overline{\Psi} + \frac{1}{2}\kappa_\eta C_{x,2}^f \cos(\phi_{\Psi_2} - \phi_{C_{x,2}^f})\Psi_2. \tag{15}$$

In (15), $\overline{C_\eta}$ depends on the time-averaged and fluctuating parts of Ψ ($\overline{\Psi}$ and Ψ_2). However, as $C_{x,2}^f$ is generally small compared to $\overline{C_x^f}$, the contribution of the term related to $\overline{\Psi}$ is expected to dominate, especially when $\overline{\Psi} \gg \Psi_2$. In this case, the model suggests a linear trend of $\overline{C_\eta}$ versus $\overline{\Psi}$:

$$\overline{C_\eta} \approx \overline{C_x^f} + \kappa_\eta \overline{C_x^f}(\overline{\Psi} - 1). \tag{16}$$

The evolution of $\overline{C_\eta}$ as a function of $\overline{\Psi} - 1$, issued from the simulations, is plotted in Fig. 10(a). In this plot, the color of the symbols indicates the relative weights of $\overline{\Psi}$ and Ψ_2: high/low values of the ratio $\overline{\Psi}/\Psi_2$ are colored in dark blue/white. The

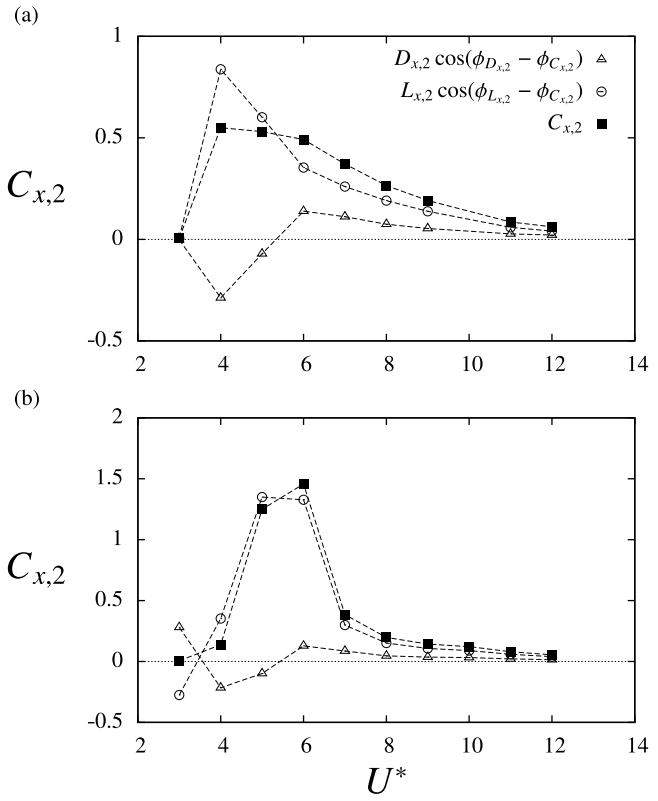

Fig. 9. Drag- and lift-like contributions to the fluctuating in-line force as functions of the reduced velocity: evolutions of the three terms in (13) in the (a) *CF* and (b) *IL+CF* cases.

linear relation suggested by (16) is generally observed when $\overline{\Psi} \gg \Psi_2$ (dark-blue symbols). As shown in Fig. 10(b), $\overline{C_x}$ is closely connected to $\overline{C_\eta}$. The increase of $\overline{C_x}$ observed when the body oscillates in one or both directions (Fig. 4(a)) can thus be related to the modulation of $\overline{C_\eta}$ by $\overline{\Psi}$.

The phenomenological model also suggests a trend for the fluid force normal to the instantaneous oncoming flow velocity, C_ξ. According to (9), the magnitude of the first harmonic can be expressed as follows:

$$\begin{aligned} C_{\xi,1} \approx & (1-\kappa_\xi) C^f_{y,1} \cos(\phi_{C^f_{y,1}} - \phi_{C_{\xi,1}}) \\ & + \kappa_\xi C^f_{y,1} \overline{\Psi} \cos(\phi_{C^f_{y,1}} - \phi_{C_{\xi,1}}) \\ & + \frac{1}{2} \kappa_\xi C^f_{y,1} \Psi_2 \sin(\phi_{C_{\xi,1}} - \phi_{\Psi_2} + \phi_{C^f_{y,1}}), \end{aligned} \tag{17}$$

where $\phi_{C_{\xi,1}}$ denotes the phase of the first harmonic of C_ξ. The third term of (17) becomes negligible when $\overline{\Psi} \gg \Psi_2$. In this case, $C_{\xi,1}$ is expected to follow a linear evolution as a function of $\overline{\Psi}$,

$$C_{\xi,1} \approx C^f_{y,1} \cos(\phi_{C^f_{y,1}} - \phi_{C_{\xi,1}}) + \kappa_\xi C^f_{y,1} \cos(\phi_{C^f_{y,1}} - \phi_{C_{\xi,1}})(\overline{\Psi} - 1). \tag{18}$$

The results reported in Fig. 11(a), which are issued from the present simulations, globally confirm this trend for $\overline{\Psi} \gg \Psi_2$ (dark-blue symbols).

As shown in Fig. 11(b), the amplification of $C_{\xi,1}$ is generally accompanied by an increase of $C_{y,1}$. Therefore, the modulation of $C_{\xi,1}$ by $\overline{\Psi}$ may play a role in the alteration of the cross-flow response when in-line oscillations occur. The structural responses are often close to harmonic. For harmonic oscillations defined as

$$\zeta_x = \zeta_{x,2} \sin(4\pi f_1 t + \phi_{\zeta_{x,2}}), \tag{19a}$$

$$\zeta_y = \zeta_{y,1} \sin(2\pi f_1 t + \phi_{\zeta_{y,1}}), \tag{19b}$$

where $\zeta_{i,n}$ are the spectral amplitudes and $\phi_{\zeta_{i,n}}$ the corresponding phases, the time-averaged value of Ψ is equal to

$$\overline{\Psi} = 1 + 2\pi^2 f_1^2 \left(4\zeta^2_{x,2} + \zeta^2_{y,1}\right). \tag{20}$$

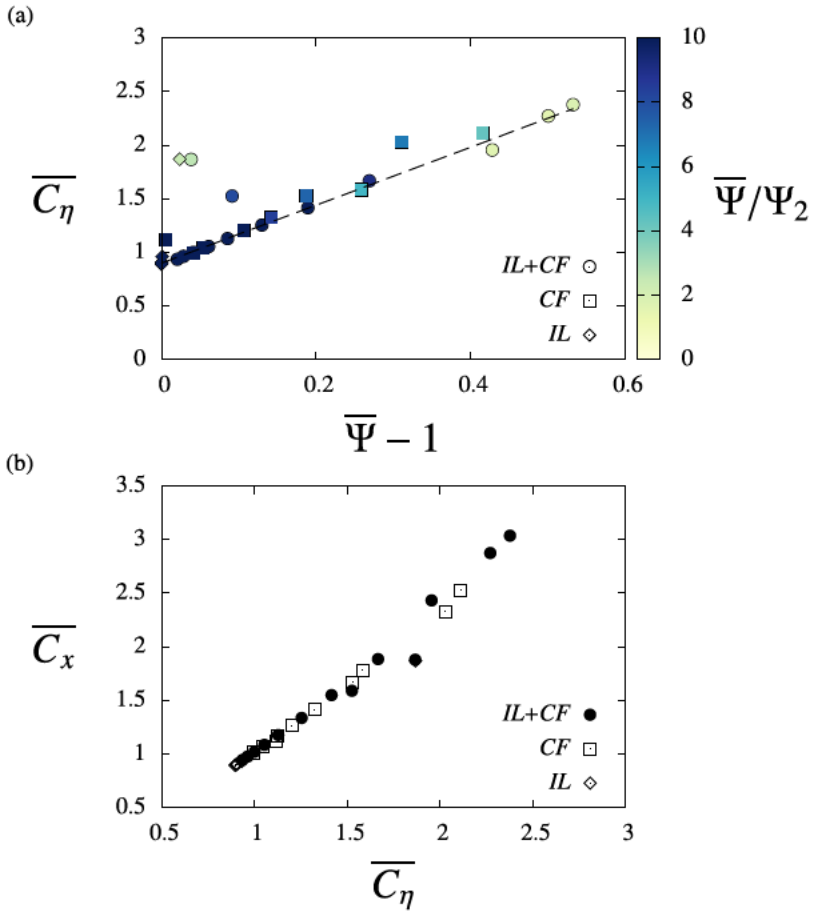

Fig. 10. Amplification of the time-averaged in-line force: (a) $\overline{C_\eta}$ as a function of $\overline{\Psi} - 1$, and (b) $\overline{C_x}$ as a function of $\overline{C_\eta}$, in the three studied cases. In (a), the symbols are colored by $\overline{\Psi}/\Psi_2$ (high/low values are colored in dark blue/white), and a dashed line indicates the general trend of the data.

Regardless the phasing between the in-line and cross-flow motions, $\overline{\Psi}$ is thus expected to increase with the in-line oscillation amplitude, which may result in an amplification of $C_{\xi,1}$ and $C_{y,1}$, and impact the cross-flow response.

4.3. Force higher harmonics

The fluid force spectra may exhibit higher harmonic components, as illustrated in Fig. 6. A large-amplitude third harmonic emerges in the cross-flow force spectrum, in two cases: in the *IL+CF* case for intermediate values of U^*, and in the *IL* case for low values of U^*. While the former has already been well documented in prior works (Jauvtis and Williamson, 2004; Vandiver et al., 2009; Dahl et al., 2010; Gsell et al., 2016), the latter has received less attention. As suggested by Dahl et al. (2007), the presence of force higher harmonics may be connected to multi-vortex shedding patterns (e.g. *2P*, *2T*). Such connection is not observed in the present results: for $U^* = 6$, a *2S* pattern is noted in the *IL+CF* case with a large-amplitude third harmonic component of C_y, while the *2P* pattern noted in the *CF* case is associated with a very low amplitude of the third harmonic component of this force. Higher harmonics may also be induced by the variations of α, as discussed by Wang et al. (2003) and Wu et al. (2012); however, this cannot explain the emergence of higher harmonics in the *IL* case, where $\alpha = 0$. The possible connection between the third harmonic of the cross-flow force and the kinematic quantities α and Ψ is further explored in the following.

The magnitude of the third harmonic of the cross-flow force can be expressed as a function of the drag- and lift-like contributions (expression (12)):

$$C_{y,3} = D_{y,3}\cos(\phi_{D_{y,3}} - \phi_{C_{y,3}}) + L_{y,3}\cos(\phi_{L_{y,3}} - \phi_{C_{y,3}}). \tag{21}$$

An analysis of the relative weights of the different terms in (21), similar to that presented in Fig. 9, shows that the drag-like contribution is negligible; the third harmonic of C_y is thus mostly induced by the lift-like contribution, which relates to C_ξ.

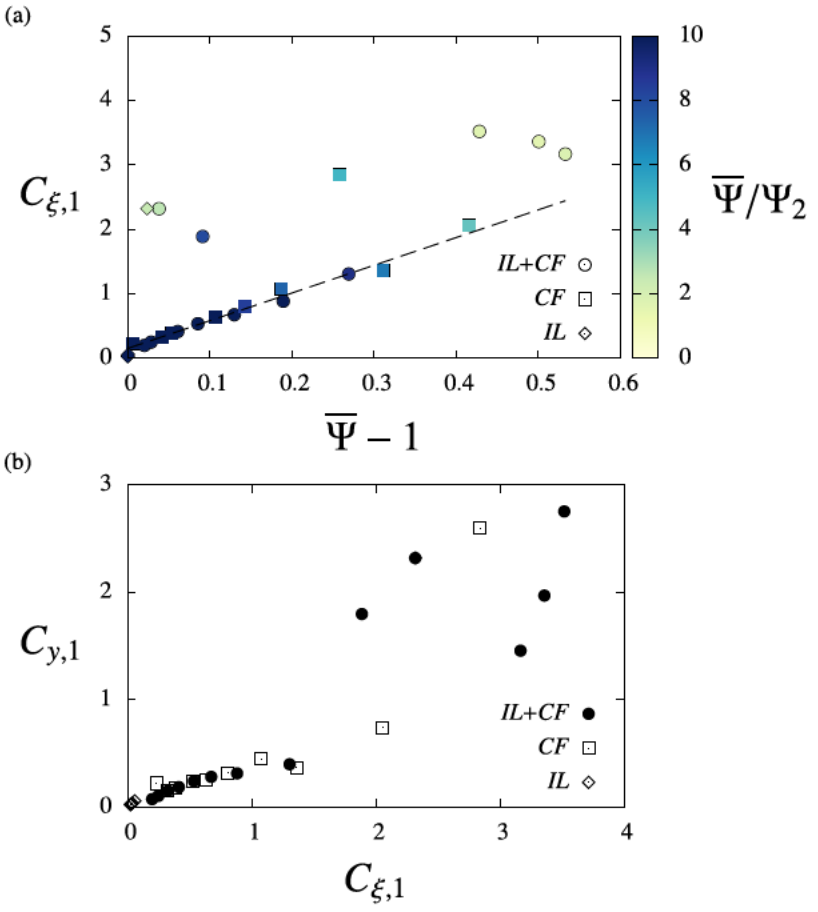

Fig. 11. Amplification of the cross-flow force fluctuation: (a) $C_{\xi,1}$ as a function of $\overline{\Psi} - 1$, and (b) $C_{y,1}$ as a function of $C_{\xi,1}$, in the three studied cases. In (a), the symbols are colored by $\overline{\Psi}/\Psi_2$ (high/low values are colored in dark blue/white), and a dashed line indicates the general trend of the data.

The phenomenological model (9) predicts the emergence of a third harmonic of C_ξ; its magnitude is expected to follow a linear trend as a function of Ψ_2:

$$C_{\xi,3} \approx \frac{1}{2}\kappa_\xi \Psi_2 C^f_{y,1}. \tag{22}$$

The evolution of $C_{\xi,3}$ as a function of Ψ_2 is plotted in Fig. 12(a). The increasing trend of $C_{\xi,3}$ with Ψ_2 is confirmed, even if it may deviate from linearity. As shown in Fig. 12(b), $C_{y,3}$ and $C_{\xi,3}$ are closely linked.

The above observations suggest that the appearance of a third harmonic in the cross-flow force can be explained by the modulation due to the variations of the instantaneous flow velocity magnitude; this mechanism is complementary to the effect of α described by Wang et al. (2003) and also applies to the *IL* case (where α vanishes). Fig. 8(b) shows that small in-line oscillations may be accompanied by a major increase of Ψ_2 (*IL* case, $U^* = 3$). Therefore, the large-amplitude third harmonic of C_y in the *IL*+*CF* case, close to $U^* = 6$, could be induced by the in-line oscillations of the body and the associated alteration of Ψ_2. It is recalled that no significant third harmonic appears in the *CF* case.

5. Summary

The one- versus two-degree-of-freedom vortex-induced vibrations of a circular cylinder have been studied over a range of reduced velocities, at $Re = 3900$, on the basis of direct numerical simulation results. Three systems have been considered: the elastically mounted cylinder was free to oscillate either in the in-line direction (*IL* case), in the cross-flow direction (*CF* case), or in both directions (*IL*+*CF* case).

In the *IL*+*CF* case, in-line and cross-flow responses significantly differ from those observed in the *IL* and *CF* cases, especially in the intermediate reduced velocity region, i.e. the range of U^* where large-amplitude cross-flow vibrations usually occur. Three features have been emphasized in this region. First, large-amplitude in-line oscillations, up to 0.3 body diameters, appear in the *IL*+*CF* case, while no vibrations develop in the *IL* case. Second, these in-line oscillations

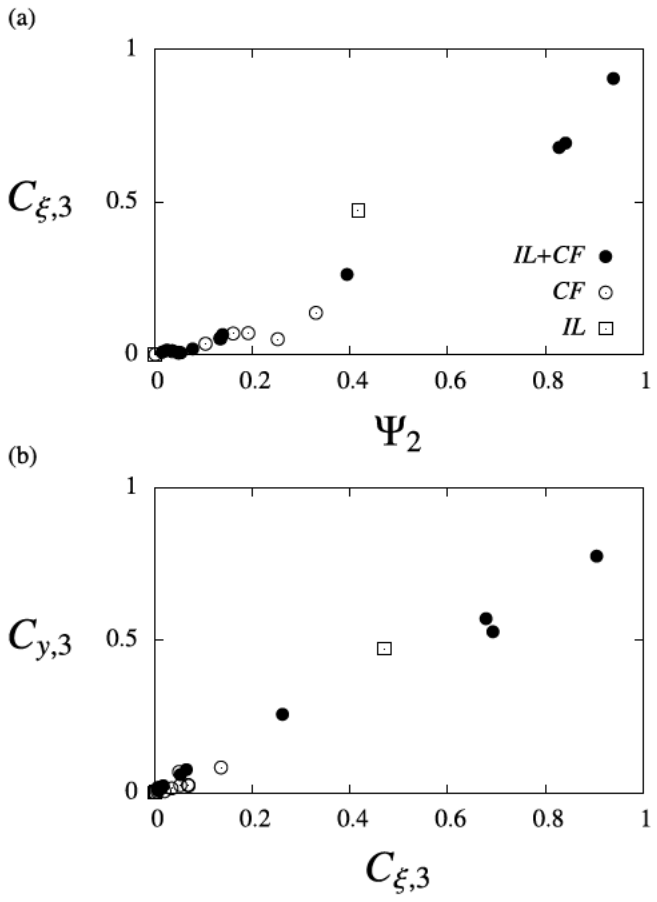

Fig. 12. Amplification of the third harmonic component of the cross-flow force: (a) $C_{\xi,3}$ as a function of Ψ_2, and (b) $C_{y,3}$ as a function of $C_{\xi,3}$, for the three studied cases.

are accompanied by a substantial increase of the cross-flow responses, compared to the *CF* case. Third, the two-degree-of-freedom responses are associated with the emergence of large-amplitude higher harmonics in the fluid force spectra; the magnitude of the third harmonic of the cross-flow force may reach 40% of the first harmonic magnitude. Even if the topology of the flow may vary from one case to the other, the differences noted in the structural responses and fluid forces do not seem to be systematically connected to wake patterns.

In order to shed some light on the above features, the fluid forces have been expressed as combinations of components parallel and normal to the instantaneous flow velocity seen by the moving body; the contributions of these components to C_x and C_y are referred to as drag-like and lift-like contributions. The major amplification of the fluctuating in-line force, noted when the body oscillates in the cross-flow direction, is essentially due to the appearance of a lift-like contribution, which does not exist in the *IL* case. This mechanism could explain the large-amplitude in-line oscillations observed in the *IL+CF* case. In addition, some connections have been established between the variations of the magnitude of the instantaneous flow velocity and the enhancement of the first and third harmonics of the instantaneously normal force. Such connections may justify the amplification of the cross-flow oscillations and of the third harmonic component of the cross-flow force when in-line oscillations occur in the *IL+CF* case.

Acknowledgments

This study is part of a Ph.D. work (S. Gsell) funded by the French Ministry of Research, France. It was performed using HPC resources from GENCI (grants x20152a7184, c20162a7184).

References

Afgan, I., Kahil, Y., Benhamadouche, S., Sagaut, P., 2011. Large eddy simulation of the flow around single and two side-by-side cylinders at subcritical reynolds numbers. Phys. Fluids 23 (7), 075101.
Aguirre, J.E., 1977. Flow induced, in-line vibrations of a circular cylinder (Ph.D thesis), Imperial College of Science and Technology.

Bearman, P.W., 1984. Vortex shedding from oscillating bluff bodies. Annu. Rev. Fluid Mech. 16 (1), 195–222.
Bishop, R.E.D., Hassan, A.Y., 1964. The lift and drag forces on a circular cylinder oscillating in a flowing fluid. Proc. R. Soc. A 277 (1368), 51–75.
Blackburn, H.M., Govardhan, R.N., Williamson, C.H.K., 2001. A complementary numerical and physical investigation of vortex-induced vibration. J. Fluids Struct. 15 (3), 481–488.
Brika, D., Laneville, A., 1993. Vortex-induced vibrations of a long flexible circular cylinder. J. Fluid Mech. 250, 481–508.
Cagney, N., Balabani, S., 2013. Wake modes of a cylinder undergoing free streamwise vortex-induced vibrations. J. Fluids Struct. 38, 127–145.
Cagney, N., Balabani, S., 2014. Streamwise vortex-induced vibrations of cylinders with one and two degrees of freedom. J. Fluid Mech. 758, 702–727.
Dahl, J.M., Hover, F.S., Triantafyllou, M.S., Dong, S., Karniadakis, G.E., 2007. Resonant vibrations of bluff bodies cause multivortex shedding and high frequency forces. Phys. Rev. Lett. 99 (14), 144503.
Dahl, J.M., Hover, F.S., Triantafyllou, M.S., Oakley, O.H., 2010. Dual resonance in vortex-induced vibrations at subcritical and supercritical reynolds numbers. J. Fluid Mech. 643, 395–424.
Feng, C.C., 1968. The measurement of vortex-induced effects in flow past stationary and oscillating circular and D-section cylinders (Master's thesis), University of British Columbia.
Govardhan, R.N., Williamson, C.H.K., 2000. Modes of vortex formation and frequency response of a freely vibrating cylinder. J. Fluid Mech. 420, 85–130.
Gsell, S., Bourguet, R., Braza, M., 2016. Two-degree-of-freedom vortex-induced vibrations of a circular cylinder at re = 3900. J. Fluids Struct. 67, 156–172.
Hover, F.S., Techet, A.H., Triantafyllou, M.S., 1998. Forces on oscillating uniform and tapered cylinders in crossflow. J. Fluid Mech. 363, 97–114.
Huera-Huarte, F.J., Bearman, P.W., 2009. Wake structures and vortex-induced vibrations of a long flexible cylinder - part 1: dynamic response. J. Fluids Struct. 25 (6), 969–990.
Jauvtis, N., Williamson, C.H.K., 2004. The effect of two degrees of freedom on vortex-induced vibration at low mass and damping. J. Fluid Mech. 509, 23–62.
Khalak, A., Williamson, C.H.K., 1997. Fluid forces and dynamics of a hydroelastic structure with very low mass and damping. J. Fluids Struct. 11 (8), 973–982.
Khalak, A., Williamson, C.H.K., 1999. Motions, forces and mode transitions in vortex-induced vibrations at low mass-damping. J. Fluids Struct. 13 (7), 813–851.
Leontini, J.S., Thompson, M.C., Hourigan, K., 2006. The beginning of branching behaviour of vortex-induced vibration during two-dimensional flow. J. Fluids Struct. 22 (6), 857–864.
Naudascher, E., 1987. Flow-induced streamwise vibrations of structures. J. Fluids Struct. 1 (3), 265–298.
Navrose, Mittal, S., 2013. Free vibrations of a cylinder: 3-d computations at Re= 1000. J. Fluids Struct. 41, 109–118.
Norberg, C., 2003. Fluctuating lift on a circular cylinder: review and new measurements. J. Fluids Struct. 17 (1), 57–96.
Okajima, A., Nakamura, A., Kosugi, T., Uchida, H., Tamaki, R., 2004. Flow-induced in-line oscillation of a circular cylinder. Eur. J. Mech. B Fluids 23 (1), 115–125.
Ouvrard, H., Koobus, B., Dervieux, A., Salvetti, M.V., 2010. Classical and variational multiscale les of the flow around a circular cylinder on unstructured grids. Comput. & Fluids 39 (7), 1083–1094.
Païdoussis, M.P., Price, S.J., de Langre, E., 2010. Fluid-Structure Interactions: Cross-Flow-Induced Instabilities. Cambridge University Press.
Sarpkaya, T., 1978. Fluid forces on oscillating cylinders. ASCE J. Waterway, Port, Coaastal, Ocean Division 104, 275–290.
Sarpkaya, T., 2004. A critical review of the intrinsic nature of vortex-induced vibrations. J. Fluids Struct. 19 (4), 389–447.
Shiels, D., Leonard, A., Roshko, A., 2001. Flow-induced vibration of a circular cylinder at limiting structural parameters. J. Fluids Struct. 15 (1), 3–21.
Vandiver, J.K., Jaiswal, V., Jhingran, V., 2009. Insights on vortex-induced, traveling waves on long risers. J. Fluids Struct. 25 (4), 641–653.
Wang, X.Q., So, R.M.C., Chan, K.T., 2003. A non-linear fluid force model for vortex-induced vibration of an elastic cylinder. J. Sound Vib. 260 (2), 287–305.
Wieselsberger, C., 1922. New data on the laws of fluid resistance. In: Tech. Rep. National Advisory Comittee for Aeronautics.
Williamson, C.H.K., Govardhan, R.N., 2004. Vortex-induced vibrations. Annu. Rev. Fluid Mech. 36, 413–455.
Williamson, C.H.K., Roshko, A., 1988. Vortex formation in the wake of an oscillating cylinder. J. Fluids Struct. 2 (4), 355–381.
Wu, X., Ge, F., Hong, Y., 2012. A review of recent studies on vortex-induced vibrations of long slender cylinders. J. Fluids Struct. 28, 292–308.